A Novel Dwell Time Modification Framework for Low Spatial Frequency Errors Suppression Under Complex Task Interactions in Optical Fabrication

Li, Jun; Cheng, Gang; Fan, Bin; Pang, Yusong

DOI
10.1109/TMECH.2025.3536465

Publication date
2025

Document Version
Final published version

Published in
IEEE/ASME Transactions on Mechatronics

Citation (APA)
Li, J., Cheng, G., Fan, B., & Pang, Y. (2025). A Novel Dwell Time Modification Framework for Low Spatial Frequency Errors Suppression Under Complex Task Interactions in Optical Fabrication. *IEEE/ASME Transactions on Mechatronics*, *30*(6), 6289-6301. https://doi.org/10.1109/TMECH.2025.3536465

IEEE/ASME TRANSACTIONS ON MECHATRONICS, VOL. 30, NO. 6, DECEMBER 2025

A Novel Dwell Time Modification Framework for Low Spatial Frequency Errors Suppression Under Complex Task Interactions in Optical Fabrication

Jun Li, *Graduate Student Member, IEEE*, Gang Cheng, Bin Fan, and Yusong Pang

***Abstract*—The manufacturing extremity and surface convergence efficiency of high-precision, large optical free-form surfaces produced through computer-controlled optical surfacing and industrial robotics face significant challenges. These challenges arise from task-related stiffness deficiencies of industrial robots and dynamic uncertainties in the tool influence function, which severely impact low spatial frequency (LSF) errors and the clarity of imaging in high-resolution optical systems. To address these issues and achieve consistent optical polishing outcomes, we propose a novel polishing dwell time modification framework. This framework is based on the spatial compliance field linked to the specific machining task and the Frenet frame, dynamically adjusting the polishing dwell time to mitigate LSF errors and enhance surface convergence efficiency. The efficacy of this modification framework was evaluated through a series of multilevel gradient experiments in Sim2Real machining environments. The experimental results show a significant reduction in low-frequency spatial errors, underscoring the potential of our approach to improve precision in high-resolution optical systems.**

***Index Terms*—Dwell time modification, low spatial frequency (LSF) errors, machining task interactions, optical fabrication.**

I. Introduction

THE high-precision, large aperture free-form surfaces are integral components of advanced space-based optical remote sensing systems, where fabrication accuracy and efficiency are paramount to achieving superior instrument performance [1], [2], [3]. Polishing, a critical step in shaping optical free-form surfaces, is highly susceptible to external perturbations that can compromise both efficiency and surface quality. The spatial frequency errors across various scales on optical surfaces lead to wavefront aberrations, ultimately constraining the optical system's performance. Among these, low spatial frequency (LSF) errors are particularly detrimental, introducing broad wavefront distortions such as image dispersion and coma. These distortions severely aggravate the point spread function and optical transfer function, both of which are essential for determining optical imaging quality and resolution [4]. LSF errors impair the system's capability to capture fine details, underscoring the necessity for precise error mitigation during polishing. Effective suppression and correction of LSF errors are critical for optimizing imaging performance in high-resolution space-based optical remote sensing systems [5]. Therefore, for most high-resolution applications, addressing LSF errors is the highest priority for achieving superior imaging quality, as demonstrated in Fig. 1.

A. Literature Review and Technical Dilemmas Statement

Conventionally, the fabrication of advanced optical surfaces has relied on large-scale optical machining centers. Recently, the industrial robots equipped with computer-controlled optical surfacing (CCOS) technology have been increasingly adopted, offering a reduced manufacturing footprint and significantly lower hardware costs [6], [7], [8]. In parallel, aiming to address the challenges of geometric complexity and stringent quality requirements in optical free-form surface fabrication, robot assisted bonnet polishing has emerged as an advanced ultraprecision technique [7], [8], [9]. Renowned for its high polishing efficiency and the eminent adaptability of the tool influence function (TIF), the technique has demonstrated significant potential for achieving nanoscale shape accuracy and surface finish on free-form surfaces [10], [11], [12].

Received 30 May 2024; revised 6 October 2024 and 29 December 2024; accepted 24 January 2025. Date of publication 20 February 2025; date of current version 30 December 2025. Recommended by Technical Editor Z. Zhu and Senior Editor D. Chen. This work was supported in part by the National Nature Science Foundation of China (NSFC) under Grant 52275039 and in part bythe Priority Academic Program Development of Jiangsu Higher Education Institutions (PAPD). *(Corresponding author: Gang Cheng.)*

Jun Li and Gang Cheng are with the School of Mechanical and Electrical Engineering, China University of Mining and Technology, Xuzhou 221116, China (e-mail: tb20050006b2@cumt.edu.cn; chg@cumt.edu.cn).

Bin Fan is with the Institute of Optics and Electronics, Chinese Academy of Sciences, Chengdu 610209, China (e-mail: fanbin@ioe.ac.cn).

Yusong Pang is with the Section of Transport Engineering and Logistics, Delft University of Technology, 2600 AA Delft, The Netherlands (e-mail: Y.Pang@tudelft.nl).

Color versions of one or more figures in this article are available at https://doi.org/10.1109/TMECH.2025.3536465.

Digital Object Identifier 10.1109/TMECH.2025.3536465

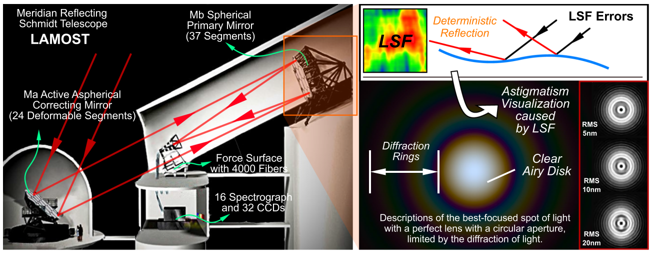

Fig. 1. High-precision optics in astronomical optical system [e.g., large sky area multi-object fiber spectroscopic telescope (LAMOST)]. Although active optics (i.e., Ma active correcting mirror) alleviates the adverse effects of wavefront aberrations to a certain extent, high-quality optics with minimal LSF errors remain a prerequisite for modern high-resolution imaging.

As a double-edged sword, the inherent flexibility of the CCOS-technique-based robots comes with a critical tradeoff—the lack and imbalance of machining stiffness compared to giant machine tools poses a substantial challenge for achieving the determinacy required in advanced optical fabrication. The critical challenge of the task is achieving consistent, high-precision manufacturing of large aperture optics under uneven task stiffness caused by complex task interactions between machining postures and the workpiece, which requires balancing the demands of maintaining high surface convergence and efficiency while thoroughly suppressing the LSF errors. Meanwhile, it is generally accepted that the dwell time distribution map heavily relies on the assumption of a constant material removal rate (MRR) as follows:

1) material removal in CCOS machining is assumed to follow a linear relationship, being directly proportional to the dwell time;

2) the TIF is generally regarded as time-invariant and independent of the robots or the optics under production [13].

Therefore, a comprehensive insight of the removal mechanism of the surface material, alongside the dependable control of the TIF's stability and the dwell time distribution, is paramount to ensuring surface quality and achieving precision shape control for realizing the deterministic optical fabrication.

In practice, the idealized assumptions of a constant TIF are often compromised by the complexities inherent in machining environments. Variables such as tool wear, the intricate interactions between the polishing tool and the optical surface, and fluctuating process conditions induce dynamic changes in the TIF. To address these challenges, researchers have made significant advancements in understanding and mitigating the effects of a dynamic TIF on deterministic polishing processes. Zhang et al. [14] examined the complex force profile governing the contact state between the polishing pad and the workpiece. Their MRR error model incorporates quasi-stress relaxation and material creep effects induced by fluctuating polishing forces, demonstrating that these effects can be alleviated through effective temperature control. Wang et al. [15] investigated the impact of pore size, density, and distribution on polyurethane polishing pads, proposing a material removal mechanism model based on the effective number of abrasive particles and the actual contact force between individual particles and the workpiece surface during polishing. Liao et al. [16] introduced a novel equilibrium equation for material removal in full-aperture polishing, directly linking surface shape to critical factors such as relative velocity, polishing pressure, and the removal coefficient, which provides valuable insights into the surface shape convergence mechanism and advances the full-aperture polishing process.

Given the negative effects of evolutionary TIF on deterministic polishing, researchers have prioritized precise material removal control by adjusting the dwell time. Huang et al. [17] simulated the stiffness of a robotic system and refined the dwell time using the Preston formula, validating the method through planar fix-point polishing experiments. Lv et al. [18] enhanced tool path optimization by incorporating a modified material removal model and machining allowance distribution, supported by a dwell time calculation model and interpolation algorithm. Ji et al. [19] developed a dwell time calculation method to address nonlinearity induced by time-varying TIF caused by plasma thermal effects, thereby improving the MRR. Wang et al. [20] proposed a dwell time compensation method that introduces a temperature-sensitive TIF to mitigate errors associated with thermal fluctuations during machining, enhancing the reliability of deterministic polishing.

Although significant progress has been made in dwell time correction methods based on evolutionary TIF consideration, the substantial part of research have primarily concentrated on disturbances caused by technology parameters, tending to lose sight of the adverse effects introduced by the processing equipment itself on surface convergence. Existing evolutionary TIF models are invariably constrained by complicated assumptions in theoretical material removal models, rendering them susceptible to external environmental disturbances during the fabrication. Consequently, utilizing a calibrated static TIF under such conditions to calculate dwell time may introduce additional surface shape errors, necessitating consideration of factors beyond the CCOS techniques. On the other hand, calculating dwell time for dynamic TIF often faces computational challenges, particularly due to the limitations of conventional 2-D deconvolution methods in handling large-scale computations. To address these challenges, a promising approach would involve incorporating the dynamic impact of processing equipment on the TIF and devising compensation methods that maintain computational efficiency. This approach aims to establish a more robust and universal framework for correcting LSF errors, ultimately improving the convergence and determinacy of high-precision optical fabrication.

B. Research Contributions and Article Organization

Considering the variable and uneven spatial task stiffness distribution inherent in industrial robots equipped with CCOS technology, coupled with the complex interactions between the robot, tools, and optics arising from diverse machining tasks, we propose a novel dwell time modification method for optical fabrication. This method leverages dynamic TIF and the Frenet frame under the contact theory to effectively suppress LSF errors. To the best of our knowledge, this represents the first effort to address these challenges in the field, with promising potential for extension to other high-precision machining scenarios involving industrial robots. The ground-breaking contributions and the critical outcomes with in this research are outlined as follows.

1) We present a generalized framework for modifying the TIF in robotic-assisted polishing, incorporating the Hertz contact model and the Navier–Stokes assumptions. To accurately characterize the dynamic evolution of the TIF during machining tasks, the proposed approach integrates a robot stiffness surrogate model with a discrete Frenet frame derived from the task trajectory.
2) This research quantifies the detrimental effects of surface errors induced by dynamic TIF variations resulting from robot stiffness deficiencies. It introduces a comprehensive tool influence matrix optimization map to correct dwell time, enabling the rapid convergence of LSF errors across the full aperture without modifying existing dwell time algorithms or requiring additional hardware.

The rest of this article is organized as follows. Section II provides a brief statement of the problem and the derivation of the stiffness surrogate model. In Section III, a generic TIF model based on the Hertz contact theory and Navier–Stokes postulates, accounting for robot stiffness defects, is developed. The novel evolutionary TIF-based dwell time modification framework is subsequently proposed. Section IV presents the implementation details of the designed hybridization experiment. Finally, Section V concludes this article.

II. PRELIMINARIES

This section initially elucidates the fundamental cause of the regenerative error stemming from the task compliance distribution characteristics inherent in the CCOS machining robot employed for polishing. Subsequently, it delves into the stiffness surrogate model pertinent to the machining robot.

A. Problem Description

Maintaining a constant normal polishing force through stable loading pressure on the actuator (i.e., the voice coil actuator here) is crucial in polishing processes. However, the inherent stiffness deficiencies of industrial robots result in undesirable deformation between the tool end and the intended contact position. While the precession angle in bonnet polishing is kept constant to maintain a stable TIF, the complex and diverse polishing trajectories required for intricate optical free-form surfaces generate multifaceted interactions among the robots, polishing tools, and workpieces. These interactions persist without altering the precession angle, thereby complicating the achievement of high-precision polishing results. The interaction between the stiffness coordinate system of the robot $\{O_T - X_T Y_T Z_T\}$ and the local contact coordinate system of the workpiece $\{\mathcal{O}(t) - \mathcal{T}(t)\mathcal{N}(t)\mathcal{B}(t)\}$ results in significant discrepancies between the TIF model and dwell time during the polishing process, as illustrated in Fig. 2. Active contact force control, which introduces additional Degrees of Freedom (DoFs) in axis movement, helps maintain a constant polishing force and mitigates derivational effects of stiffness variations in robots. However, this approach suppresses the effects of stiffness changes in the actuator axis alone. The resultant force, decomposed from the workpiece support force on the plane XOY, is influenced by the mismatch of dwell time, resulting from varying tool penetration depths into the optical surface (i.e., the TIF here) under the task-related, time-varying normal contact stiffness, resulting in deviations in material removal. Such deviations are particularly detrimental in high-precision optical free-form machining, as they introduce LSF errors that are repeatedly left and perpetuated during subsequent polishing stages due to the robot stiffness limitations and the lack of effective compensation in the current setup, thereby threatening the efficiency of the high-precision optical finishing phase.

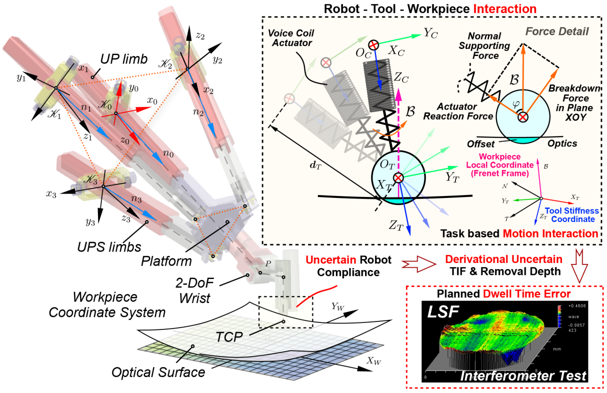

Fig. 2. Illustration of the robot–tool–workpiece interaction. The dynamic TIF is one of the significant causes for the LSF errors during the high-precision optical polishing. Despite maintaining a constant included angle between the tool axis and the optical surface normal throughout the machining process, motion interaction with the optical surface can still be achieved through the remaining 2 DoF within the defined stiffness coordinate system.

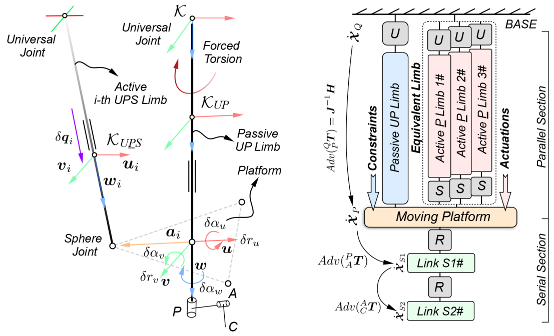

Fig. 3. Coordinate definition of the stiffness surrogate model.

B. System Stiffness Formulation

As presented in Fig. 3, the kinematic correlation between the moving platform and the limbs within the parallel segment of the hybrid robot can be delineated as follows:

$$\boldsymbol{r} = \boldsymbol{b}_i + q_i \boldsymbol{w}_i - \boldsymbol{a}_i = \sqrt{\boldsymbol{r}^{\mathrm{T}} \boldsymbol{r}}\,\boldsymbol{w} \tag{1}$$

where $\boldsymbol{r}$ and q_i denote the vector from the base to the moving platform center and the ith active limb length, respectively. Thus, the relationship between velocity vectors of the active limbs and the moving platform via the differentiation with respect to time of (1) can be defined as follows:

$$\boldsymbol{J}_a^{\mathrm{T}}\dot{\boldsymbol{\mathcal{X}}} = \dot{\boldsymbol{q}}, \boldsymbol{J}_a = \begin{bmatrix} \boldsymbol{w}_1 & \boldsymbol{w}_2 & \boldsymbol{w}_3 \\ \boldsymbol{a}_1 \times \boldsymbol{w}_1 & \boldsymbol{a}_2 \times \boldsymbol{w}_2 & \boldsymbol{a}_3 \times \boldsymbol{w}_3 \end{bmatrix} \tag{2}$$

where $\dot{\boldsymbol{q}}$ and $\dot{\boldsymbol{\mathcal{X}}} = [\dot{\boldsymbol{r}} \quad \Omega]$ denote the linear velocity vectors of the active limbs and the velocity twist of the moving platform, respectively. $\boldsymbol{w}_i$ represents the unit direction vector of the ith active limb. Since the UP limb exists, the motion constraints on the moving platform can be expressed as follows:

$$\boldsymbol{u}^{\mathrm{T}}\dot{\boldsymbol{r}} - \sqrt{\boldsymbol{r}^{\mathrm{T}}\boldsymbol{r}}\boldsymbol{v}^{\mathrm{T}}\boldsymbol{\Omega} = 0, \boldsymbol{v}^{\mathrm{T}}\dot{\boldsymbol{r}} + \sqrt{\boldsymbol{r}^{\mathrm{T}}\boldsymbol{r}}\boldsymbol{u}^{\mathrm{T}}\boldsymbol{\Omega} = 0 \tag{3}$$

where $\boldsymbol{u}$, $\boldsymbol{v}$, and $\boldsymbol{w}$ denote the unit direction vectors of the platform. The Jacobian of constraints in parallel section yields

$$\boldsymbol{J}_c^{\mathrm{T}}\dot{\boldsymbol{\mathcal{X}}} = \boldsymbol{0}_{3\times 1}, \boldsymbol{J}_c = \begin{bmatrix} \boldsymbol{u} & \boldsymbol{v} & \boldsymbol{0}_{3\times 1} \\ -\sqrt{\boldsymbol{r}^{\mathrm{T}}\boldsymbol{r}}\boldsymbol{v} & \sqrt{\boldsymbol{r}^{\mathrm{T}}\boldsymbol{r}}\boldsymbol{u} & \boldsymbol{n} \end{bmatrix} \tag{4}$$

$$\begin{bmatrix} \boldsymbol{J}_a & \boldsymbol{J}_c \end{bmatrix}^{\mathrm{T}} \dot{\boldsymbol{\mathcal{X}}} = \begin{bmatrix} \dot{\boldsymbol{q}} & \boldsymbol{0}_{1\times 3} \end{bmatrix}^{\mathrm{T}}. \tag{5}$$

Considering the compliance between the active and passive sections, the kinematic perturbation of sections is as follows:

$$\begin{aligned} &\text{Actuations.} \quad \boldsymbol{w}_i^{\mathrm{T}}\partial\boldsymbol{r} + (\boldsymbol{a}_i \times \boldsymbol{w}_i)^{\mathrm{T}}\partial\boldsymbol{\alpha} = \partial\boldsymbol{q}_i \\ &\text{Const.} \begin{cases} \boldsymbol{u}^{\mathrm{T}}\partial\boldsymbol{r} - \sqrt{\boldsymbol{r}^{\mathrm{T}}\boldsymbol{r}}\boldsymbol{v}^{\mathrm{T}}\partial\boldsymbol{\alpha} = \partial r_u - \sqrt{\boldsymbol{r}^{\mathrm{T}}\boldsymbol{r}}\partial\alpha_v \\ \boldsymbol{v}^{\mathrm{T}}\partial\boldsymbol{r} - \sqrt{\boldsymbol{r}^{\mathrm{T}}\boldsymbol{r}}\boldsymbol{u}^{\mathrm{T}}\partial\boldsymbol{\alpha} = \partial r_v - \sqrt{\boldsymbol{r}^{\mathrm{T}}\boldsymbol{r}}\partial\alpha_u \\ \boldsymbol{n}^{\mathrm{T}}\partial\boldsymbol{\alpha} = \partial\alpha_u\boldsymbol{n}^{\mathrm{T}}\boldsymbol{u} + \partial\alpha_w\boldsymbol{n}^{\mathrm{T}}\boldsymbol{w} \end{cases} \end{aligned} \tag{6}$$

where $\partial\boldsymbol{r}$ and $\partial\boldsymbol{\alpha}$ represent the elements within the deflection twist of the platform. Meanwhile, the end deflection angle and offset satisfy the linear condition, provided that the passive UP limb can be regarded as a Bernoulli beam here

$$\begin{pmatrix} \partial\alpha_u & \partial\alpha_v \end{pmatrix}^{\mathrm{T}} = \boldsymbol{W} \begin{pmatrix} \partial r_u & \partial r_v \end{pmatrix}^{\mathrm{T}}. \tag{7}$$

Thus, (6) and (7) can be rewritten as a whole as follows:

$$\begin{gathered} \boldsymbol{J}\partial\boldsymbol{\mathcal{X}}_P = \boldsymbol{H}\partial\boldsymbol{\mathcal{X}}_Q \\ \boldsymbol{J} = \begin{bmatrix} \boldsymbol{J}_a \\ \boldsymbol{J}_c \end{bmatrix}^{\mathrm{T}}, \boldsymbol{H} = \begin{bmatrix} \boldsymbol{E}^3 & \\ & \boldsymbol{S}_c \end{bmatrix}, \boldsymbol{\mathcal{X}}_P = \begin{bmatrix} \partial\boldsymbol{r} \\ \partial\boldsymbol{\alpha} \end{bmatrix}, \boldsymbol{\mathcal{X}}_Q = \begin{bmatrix} \partial\boldsymbol{q} \\ \partial\boldsymbol{\rho} \end{bmatrix} \\ \boldsymbol{S}_c = \begin{bmatrix} (1 - \sqrt{\boldsymbol{r}^{\mathrm{T}}\boldsymbol{r}})W_{11} & -\sqrt{\boldsymbol{r}^{\mathrm{T}}\boldsymbol{r}}W_{12} & 0 \\ -\sqrt{\boldsymbol{r}^{\mathrm{T}}\boldsymbol{r}}W_{21} & 1 - \sqrt{\boldsymbol{r}^{\mathrm{T}}\boldsymbol{r}}W_{22} & 0 \\ \boldsymbol{n}^{\mathrm{T}}\boldsymbol{u}W_{11} & \boldsymbol{n}^{\mathrm{T}}\boldsymbol{u}W_{12} & \boldsymbol{n}^{\mathrm{T}}\boldsymbol{w} \end{bmatrix} \in \Re^{3\times 3} \end{gathered} \tag{8}$$

where $\boldsymbol{\mathcal{X}}_P$ and $\boldsymbol{\mathcal{X}}_Q$ denote the generalized micromotion of the platform and limbs under the twist. According to the generalized definition of stiffness, the relationship between the infinitesimal external force (wrench) exerted upon the platform and the corresponding infinitesimal deflection twist yields

$$\partial\boldsymbol{F}_P = \boldsymbol{K}_P\partial\boldsymbol{\mathcal{X}}_P \tag{9}$$

where $\boldsymbol{K}_P$ denotes the stiffness of the parallel section. Using the virtual work principle, we obtain the equilibrium equation

$$\partial\boldsymbol{\mathcal{X}}_P{}^{\mathrm{T}}\partial\boldsymbol{F} + \partial\boldsymbol{\mathcal{X}}_Q{}^{\mathrm{T}}\partial\boldsymbol{T} = 0. \tag{10}$$

Assuming linear elasticity for each segment, thus

$$\boldsymbol{T} = -\boldsymbol{K}_Q\partial\boldsymbol{\mathcal{X}}_Q, \boldsymbol{K}_Q = \mathrm{Diag}[\boldsymbol{K}_a \ \boldsymbol{K}_c] \tag{11}$$

where $\boldsymbol{K}_a$ and $\boldsymbol{K}_a$ represent the component stiffness matrices of the actuations and constraints. Substitution of (8) and (11) into (10) gives the parallel section stiffness matrix

$$\begin{aligned} \boldsymbol{K}_P = \frac{\partial\boldsymbol{F}_P}{\partial\boldsymbol{\mathcal{X}}_P} &= (\boldsymbol{H}^{\dagger}\boldsymbol{J})^{\mathrm{T}} \begin{bmatrix} \boldsymbol{K}_a & \\ & \boldsymbol{K}_c \end{bmatrix} (\boldsymbol{H}^{\dagger}\boldsymbol{J}) \\ &= \mathrm{Adv}^{\mathrm{T}}({}_O^P\boldsymbol{T})\boldsymbol{K}_Q\mathrm{Adv}({}_O^P\boldsymbol{T}) \end{aligned} \tag{12}$$

where $\mathrm{Adv}({}_i^j\boldsymbol{T})$ represents the adjoint transformations of $\boldsymbol{T}_i$ w.r.t. $\boldsymbol{T}_j$. Neglecting the bending deflection as well as torsional stiffness of the beam in series section, and taking into account only the torsional stiffness of the drive part of the series section, the kinematics of the series section yields

$$\mathrm{Adv}({}_C^P\boldsymbol{T}) = \mathrm{Adv}({}_A^P\boldsymbol{T})\mathrm{Adv}({}_C^A\boldsymbol{T}) = \begin{bmatrix} {}_C^P\boldsymbol{R} & \overrightarrow{PC}^{\wedge}{}_C^P\boldsymbol{R} \\ \boldsymbol{0} & {}_C^P\boldsymbol{R} \end{bmatrix}. \tag{13}$$

Assuming that the motor-driven torsional stiffness of the series section are $\boldsymbol{K}_{S1}$ and $\boldsymbol{K}_{S2}$, respectively, the overall stiffness express of the series section can be described as

$$\boldsymbol{K}_S^{\dagger} = \mathrm{Sum}\left\{ \begin{matrix} [\mathrm{Adv}^{\mathrm{T}}({}_C^P\boldsymbol{T})\boldsymbol{K}_{S1}\mathrm{Adv}({}_C^P\boldsymbol{T})]^{\dagger}, \\ [^{\mathrm{T}}({}_P^O\boldsymbol{T})\boldsymbol{K}_{S2}({}_C^A\boldsymbol{T})]^{\dagger} \end{matrix} \right\}. \tag{14}$$

Thus, the consideration of the parallel section as an equivalent limb results in the general stiffness matrix of the whole system

$$\boldsymbol{K}_G = \{[\mathrm{Adv}^{\mathrm{T}}({}_P^C\boldsymbol{T})\boldsymbol{K}_P\mathrm{Adv}({}_P^C\boldsymbol{T})]^{\dagger} + \boldsymbol{K}_S^{\dagger}\}^{\dagger}. \tag{15}$$

III. PROPOSED METHODOLOGY

In this section, we initially investigate the material removal mechanism due to polishing pressure and the motion of the bonnet tool, with the goal of generating a generic TIF framework for dynamic machining processes, considering the effects of robot stiffness deficiencies. Subsequently, our focus shifts to explicitly defining the derivative impact of varying task compliance on optical polishing. Ultimately, we address the aforementioned uncertainties caused by the dynamic TIF through the application of a dwell time correction solution.

A. Material Removal Mechanism

During the bonnet polishing, the TIF model is determined by the stress distribution $p(x, y, t)$ and the velocity field $v(x, y, t)$ within the contact zone, following the *Preston formula* [13]:

$$dz = k\int_0^t p(x, y, t)v(x, y, t)dt. \tag{16}$$

The physical removal process of optical polishing in CCOS is demonstrated in Fig. 4. The ball-end polishing tool, propelled by a hybrid robot, rotates at high velocity across an optical

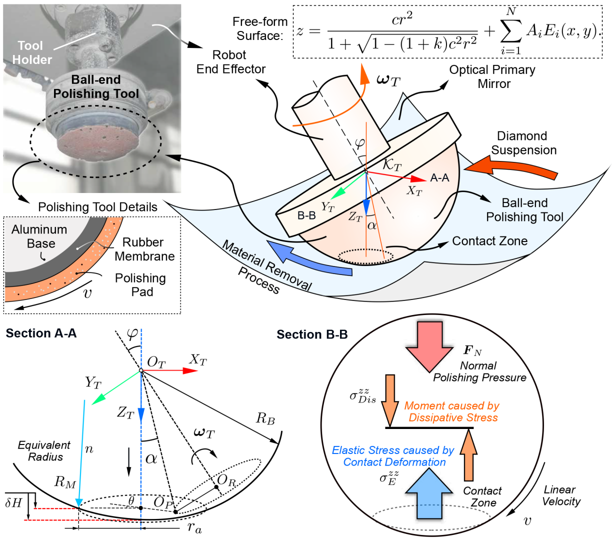

Fig. 4. Diagram for the motion details of the polishing tool and the physical material removal process, with *Section A-A* and *Section B-B*.

free-form surface. Material removal from the surface occurs deterministically through both normal polishing pressure and the application of a fine-grained CeO_2 suspension. *Sections A-A* and *B-B* illustrate the modeling of polishing speed and force exerted on the ball-end tool, respectively. The unit direction vector $\boldsymbol{\Omega}_{\text{Dir}}$ of rotational angular velocity of the ball-end tool $\boldsymbol{\Omega}_T$, as shown in *Section A-A*, can be stated as

$$\boldsymbol{\Omega}_{\text{Dir}} = \boldsymbol{\Omega}_T/\|\boldsymbol{\Omega}_T\|,\ \boldsymbol{\Omega}_{Dir} \perp \left(\text{OProj}_{\boldsymbol{\Omega}_{Dir}} \overrightarrow{O_T O_P}\right) \tag{17}$$

where φ and OProj denotes the deflection angle of the tool axis with respect to the normal direction and the vector rejection. By employing the orthogonality relation in (17) and taking into account that the radius of the tool R_B is significantly smaller compared to the equivalent radius of the free-form, the velocity field within the contact zone yields

$$\begin{aligned} \boldsymbol{V}_P &= \boldsymbol{\Omega}_T \times \overrightarrow{O_T O_P} = \mathcal{K}(\boldsymbol{\Omega}_T, \alpha, \varphi, \theta, d) \\ \overrightarrow{O_T O_P} &= \begin{pmatrix} d\tan\alpha\cos\theta & d\tan\alpha\sin\theta & d \end{pmatrix}^{\text{T}} \end{aligned} \tag{18}$$

where $d = |\overrightarrow{O_T O_M}| = R_B - \delta H$. The symbols δH and $\mathcal{K}(\cdot)$ denote the maximum depth of contact zone and the kinematics function of the input vector, respectively.

B. Physical Field-Based Contact Model: Pressure Outline

The presence of polishing force causes elastic deformation of ball-end polishing tools, resulting in material removal characterized by a displacement field. In cases where the deformation of a sphere is relatively small, the rolling velocity is significantly lower than the sound speed in the material, and the characteristic time is significantly greater than the material's dissipative relaxation time. We assume that the viscoelastic sphere follows the *Navier–Stokes postulates* [22], as demonstrated in Fig. 5

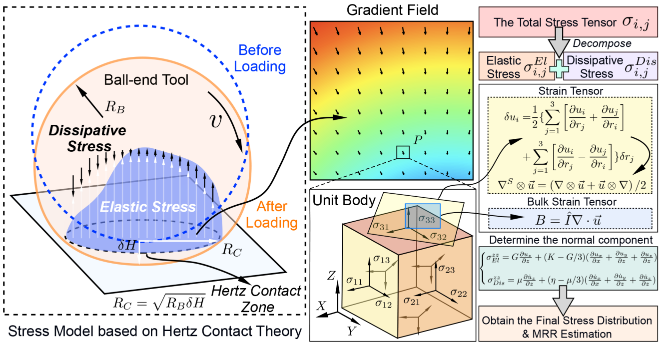

Fig. 5. Physical field illustration of the polishing zone for TIF modeling, based on the Hertz contact theory and Navier–Stokes postulates.

$$\begin{matrix}\text{Navier–Stokes} \\ \text{Postulates}\end{matrix} : \begin{cases} \vec{\sigma} = \mathscr{L}(\vec{\epsilon}). & \text{Linear stress yields.} \\ \text{fluid}(\mathscr{L}): & \text{Isotropic.} \\ \vec{\sigma} \to \text{p}. & \text{While at rest.} \end{cases}$$

Upon considering the initial position vectors of $\vec{r}$ and $\vec{r} + \delta\vec{r}$, the alteration in displacement between these two reference points is given according to the deformation $\vec{u}(r)$

$$\delta u(r) = \delta r \nabla u(r) + \mathcal{O}(\delta r^2), \delta u_i = \textstyle\sum_{j=1}^{3} \delta r_j \partial u_i/\partial r_j. \tag{19}$$

Furthermore, decomposing the right terms into symmetric and antisymmetric parts, then defining dimensionless second-order symmetric tensors ε, its tensor element satisfies

$$\delta u_i = \frac{1}{2}\left\{\sum_{j=1}^{3}\left[\frac{\partial u_i}{\partial r_j} + \frac{\partial u_j}{\partial r_i}\right] + \sum_{j=1}^{3}\left[\frac{\partial u_i}{\partial r_j} - \frac{\partial u_j}{\partial r_i}\right]\right\}\delta r_j. \tag{20}$$

$$\varepsilon_{ij} = \left[\partial u_i/\partial r_j + \partial u_j/\partial r_i\right]/2 = \varepsilon_{ji}. \tag{21}$$

The total stress tensor $\sigma_{i,j}$ comprises the sum of the elastic component $\sigma^{\text{El}}_{i,j}$ and the dissipative component $\sigma^{\text{Dis}}_{i,j}$ as follows:

$$\sigma_{i,j} = \text{Sum}\{\sigma^{\text{El}}_{i,j}, \sigma^{\text{Dis}}_{i,j}\}. \tag{22}$$

The elastic stress tensor can be obtained with elastic constants along with the displacement field $\vec{u}$ and the symmetric tensor field of the deformation $\nabla^S \otimes \vec{u}$, where $G = E/2(1+\nu)$, $K = E/3(1-2\nu)$, and $\hat{I}$ denote the shear modulus, bulk modulus, and unit tensor, respectively. Thus, the elastic stress tensor gets

$$\sigma^{\text{El}}_{i,j} = G\left[\nabla^S \otimes \vec{u} - (\hat{I}\nabla \cdot \vec{u})/3\right] + K(\hat{I}\nabla \cdot \vec{u}/3) \tag{23}$$

where $\nabla^S \otimes \vec{u} = (\nabla \otimes \vec{u} + \vec{u} \otimes \nabla)/2$. Here, E_r and ν_r are the Young's modulus and Poisson's ratio of the tool material. While, with the shear viscosity coefficient and the velocity gradient, the dissipative stress tensor yields

$$\sigma^{\text{Dis}}_{i,j} = \mu\left[(\nabla^S \otimes \dot{\vec{u}}) - (\hat{I}\nabla \cdot \dot{\vec{u}})/3\right] + \eta(\hat{I}\nabla \cdot \dot{\vec{u}}/3) \tag{24}$$

where μ and η denote the viscosity and the second viscosity of the ball-end polishing tool. The displacement velocity field

$\dot{\vec{u}} = \{\dot{u}_x, \dot{u}_y, \dot{u}_z\}$ can be further represented as follows:

$$\dot{\vec{u}}(\vec{r}) = \vec{\Omega} \cdot (\vec{r} \times \vec{\nabla})\vec{u}(\vec{r}). \tag{25}$$

Let σ_{El}^{zz}, σ_{Dis}^{zz} denote the diagonal component of $\sigma_{i,j}^{\text{El}}$ and $\sigma_{i,j}^{\text{Dis}}$ onto the z-axis, which can be further expressed as

$$\begin{cases} \sigma_{\text{El}}^{zz} = G\frac{\partial u_z}{\partial z} + (K - G/3)(\frac{\partial u_x}{\partial x} + \frac{\partial u_y}{\partial z} + \frac{\partial u_z}{\partial z}) \\ \sigma_{\text{Dis}}^{zz} = \mu\frac{\partial \dot{u}_z}{\partial z} + (\eta - \mu/3)(\frac{\partial \dot{u}_x}{\partial x} + \frac{\partial \dot{u}_y}{\partial z} + \frac{\partial \dot{u}_z}{\partial z}) \end{cases}. \tag{26}$$

According to the Hertzian contact theory [21], the diagonal component σ_{El}^{zz} in the contact zone can be alternately yields

$$\sigma_{\text{El}}^{zz}(x, y, z = z_p) = 3\sqrt{1 - (x^2 + y^2)/R_C^2 F_{\text{El}}^N}\ /2S_c \tag{27}$$

where $R_C = \sqrt{R_B \delta H}$ and F_{El}^N represents the contact zone radius and the total elastic force acting on the ball-end tool, respectively, which can be further expressed as follows:

$$\begin{aligned} F_{\text{El}}^N &= 4E^* R_B^{1/2} \delta H^{3/2}/3 \\ 1/E^* &= (1 - \nu_R^2)/E_R + (1 - \nu_r^2)/E_r \end{aligned} \tag{28}$$

where E_R, ν_R, E_r, and ν_r are the elastic constants of the optic surface and the polishing pad. Replacing G and K with μ and η, the diagonal component of $\sigma_{i,j}^{\text{Dis}}$ onto the z-axis in the transformed coordinates yields, matching with the viscosity μ, η, and Lamé's first parameter $\lambda = E\nu/[(1 + \nu)(1 - 2\nu)]$, the following:

$$\sigma_{\text{El}}^{zz}(\mu, \eta) = 3\alpha\sqrt{1 - (x^2 + y^2)/R_C^2 F_{\text{El}}^N}\ /2S_c. \tag{29}$$

Here, $\alpha = (2\eta + \mu/3)\nu/\lambda = (1 + \nu)(1 - 2\nu)(2\eta + \mu/3)/E^*$. To obtain the diagonal component of the σ_{Dis}^{zz}, the necessary preliminary is represented as follows:

$$\dot{\vec{u}} = [\omega \sin\varphi(y\partial z - z\partial y) + \omega\cos\varphi(x\partial y - y\partial x)]\vec{u}. \tag{30}$$

The displacement $\vec{u_z}(r)$ in the vertical direction due to deformation can be expressed as

$$u_z(r) = 3F_{\text{El}}^N(1 - \nu^2)(2R_C^2 - x^2 - y^2)/(8E^* R_C^3). \tag{31}$$

Substituting (29)–(31) into (26) and neglecting higher order terms, the further express of σ_{Dis}^{zz} yields

$$\begin{aligned} \sigma_{\text{Dis}}^{zz} &= \omega\text{Sum}\begin{Bmatrix} \sin\varphi(y\partial z - z\partial y) \\ \cos\varphi(x\partial y - y\partial x) \end{Bmatrix} \sigma_{\text{El}}^{zz}(\mu, \eta) \\ &\quad + (\eta - \mu/3)\omega\sin\varphi\partial y u_z(r). \end{aligned} \tag{32}$$

Thus, the total external load for polishing and the general stress distribution σ_G^{zz} within the contact integral zone S_c, yields

$$\vec{F} = -\vec{n}\iint_{S_c} \sigma_G^{zz} dxdy,\ M = \iint_{S_c} x\sigma_G^{zz} dxdy. \tag{33}$$

C. Complex Machining Task Interactions-Based Dynamic TIF

In this section, the complete definition of the task compliance based on the Frenet frame is detailed, followed by a framework for the offline correction of the dwell time. The Frenet frame is defined on a curve in $\Re^3$ space, where the coordinates of points on the curve are denoted as $\boldsymbol{\zeta}$. Assuming the general form, the tangent unit vector $\mathcal{T}\{\boldsymbol{\tau}(t)\}$ of the continuous polishing trajectory $\hat{\boldsymbol{\zeta}}(t) = \boldsymbol{\zeta}(s(t))$, yields

$$\boldsymbol{\tau}(s(t)) = \boldsymbol{\zeta}'(s(t)) = \frac{\mathrm{d}\boldsymbol{\zeta}}{\mathrm{d}t}\frac{\mathrm{d}t}{\mathrm{d}s} = \dot{\boldsymbol{\zeta}}(t)/|\dot{\boldsymbol{\zeta}}(t)|_{\Re^3}. \tag{34}$$

The preliminary, based on the definition of the principal normal vector $\boldsymbol{n}(s) = \boldsymbol{\zeta}''(s)/|\boldsymbol{\zeta}''(s)|_{\Re^3}$, is illustrated as follows:

$$\begin{aligned} \boldsymbol{\zeta}''(s(t)) &= \frac{\mathrm{d}\boldsymbol{\tau}}{\mathrm{d}t}\frac{\mathrm{d}t}{\mathrm{d}s} = \left(\frac{\mathrm{d}}{\mathrm{d}t}\dot{\boldsymbol{\zeta}}(t)/|\dot{\boldsymbol{\zeta}}(t)|_{\Re^3}\right)/|\dot{\boldsymbol{\zeta}}(t)|_{\Re^3} \\ &= \ddot{\boldsymbol{\zeta}}(t)/|\dot{\boldsymbol{\zeta}}(t)|_{\Re^3}^2 - \frac{\mathrm{d}}{\mathrm{d}t}|\dot{\boldsymbol{r}}(t)|_{\Re^3}\dot{\boldsymbol{\zeta}}(t)/|\dot{\boldsymbol{\zeta}}(t)|_{\Re^3}^3 \end{aligned} \tag{35}$$

$$\mathrm{d}|\dot{\boldsymbol{\zeta}}(t)|_{\Re^3}/\mathrm{d}t = \left(\ddot{\boldsymbol{\zeta}}(t), \dot{\boldsymbol{\zeta}}(t)\right)_{\Re^3}/|\dot{\boldsymbol{\zeta}}(t)|_{\Re^3}. \tag{36}$$

Thereupon, according to (35) and (36) and the implicit orthogonal decomposition, the normal vector $\mathcal{N}\{\boldsymbol{n}(t)\}$ obtains

$$\boldsymbol{n}(t) = \frac{\boldsymbol{\zeta}''(s(t))}{|\boldsymbol{\zeta}''(s(t))|_{\Re^3}} = -\frac{\dot{\boldsymbol{\zeta}}(t) \times (\dot{\boldsymbol{\zeta}}(t) \times \ddot{\boldsymbol{\zeta}}(t))}{|\dot{\boldsymbol{\zeta}}(t)|_{\Re^3}|\dot{\boldsymbol{\zeta}}(t) \times \ddot{\boldsymbol{\zeta}}(t)|_{\Re^3}}. \tag{37}$$

Thus, the binormal vector $\mathcal{B}\{b(t), b(t)\perp\tau(t)\&n(t)\}$, yields

$$\begin{aligned} \boldsymbol{b}(t) &= \frac{\dot{\boldsymbol{\zeta}}(t)}{|\dot{\boldsymbol{\zeta}}(t)|_{\Re^3}^3} \times \left[\ddot{\boldsymbol{\zeta}}(t) - \left(\ddot{\boldsymbol{\zeta}}(t), \frac{\dot{\boldsymbol{\zeta}}(t)}{|\dot{\boldsymbol{\zeta}}(t)|_{\Re^3}}\right)\frac{\dot{\boldsymbol{\zeta}}(t)}{|\dot{\boldsymbol{\zeta}}(t)|_{\Re^3}}\right] \\ &= \dot{\boldsymbol{\zeta}}(t) \times \ddot{\boldsymbol{\zeta}}(t)/|\dot{\boldsymbol{\zeta}}(t)|_{\Re^3}^3. \end{aligned} \tag{38}$$

To reduce the computational burden of discrete calculating the Frenet frame from complex optical free form, we obtain the planned discrete trajectory point data directly from the robot's RNC machining files. For discrete dwell point setup in the trajectory, the central difference method was utilized to offline compute the binormal vectors $\mathcal{B}\{\boldsymbol{b}_i, i = 1, 2, 3\ldots\}$. Meanwhile, the Cartesian compliance matrix for any reference pose of the dwell point can be derived from the stiffness model in (15). Thus, the Cartesian compliance matrix C_G yields

$$\begin{aligned} \boldsymbol{C}_G = \boldsymbol{K}_G^{\dagger} &= \{[\text{Adv}^{\dagger}({}_P^C\boldsymbol{T})\boldsymbol{K}_P\text{Adv}({}_P^C\boldsymbol{T})]^{\dagger} + \boldsymbol{K}_S^{\dagger}\}, \\ &= \begin{bmatrix} \boldsymbol{C}_{\text{Trans}} & \boldsymbol{C}_{\text{Cou}} \\ \boldsymbol{C}_{\text{Cou}}^{\text{T}} & \boldsymbol{C}_{\text{Rot}} \end{bmatrix} \in \Re^{6\times 6} \end{aligned} \tag{39}$$

where the $\boldsymbol{C}_{\text{Trans}}$, $\boldsymbol{C}_G^{\text{Rot}}$, and $\boldsymbol{C}_G^{\text{Cou}}$ represent the translational, the rotational, and the coupling compliance submatrices, respectively. Consequently, the line deformation $\boldsymbol{\delta}_{\text{Trans}}$ and angular deformation $\boldsymbol{\delta}_{\text{Rot}}$ at the end can be sufficiently explained by the translational force factor $\boldsymbol{F}$, as demonstrated in Fig. 6(a) as follows:

$$\boldsymbol{\delta}_{\text{Tran}} = \boldsymbol{C}_{\text{Tran}}\boldsymbol{F},\ \boldsymbol{\delta}_{\text{Rot}} = \boldsymbol{C}_{\text{cou}}^{\text{T}}\boldsymbol{F}. \tag{40}$$

Thus, the combined deformation can be expressed as

$$\boldsymbol{\delta}_{\text{Mix}} = \boldsymbol{\delta}_{\text{Tran}} - \boldsymbol{d}_T{}^{\wedge}\boldsymbol{\delta}_{\text{Rot}} = (\boldsymbol{C}_{\text{Tran}} - \boldsymbol{d}_T{}^{\wedge}\boldsymbol{C}_{\text{cou}}^{\text{T}})\boldsymbol{F} \tag{41}$$

where the defined full rank equivalent compliance matrix $\mathscr{C} = \boldsymbol{C}_{\text{Tran}} - \boldsymbol{d}_T{}^{\wedge}\boldsymbol{C}_{\text{cou}}^{\text{T}}$ satisfies the following conditions:

$$\mathscr{C}\mathscr{X}_i = \lambda_i\mathscr{X}_i, i = 1, 2, 3 \tag{42}$$

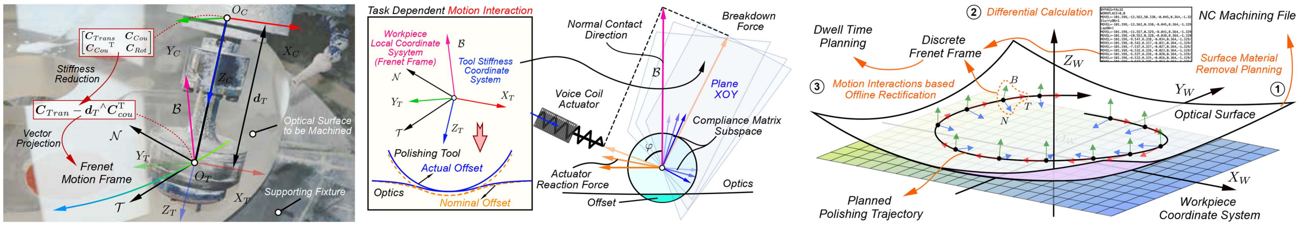

```
BYPASS=FALSE
WORKPLACE=0,0
MOVEL=-101.198,-12.562,50.330,-0.045,0.364,-1.32
SlurryON=1
MOVEL=-101.198,-12.562,0.330,-0.045,0.364,-1.329
LapON=1
MOVEL=-101.198,-11.557,0.329,-0.041,0.364,-1.329
MOVEL=-101.198,-10.552,0.328,-0.038,0.364,-1.329
MOVEL=-101.198,-9.547,0.328,-0.034,0.364,-1.329/
MOVEL=-101.198,-8.542,0.327,-0.031,0.364,-1.329/
MOVEL=-101.198,-7.537,0.327,-0.027,0.364,-1.329/
MOVEL=-101.198,-6.532,0.326,-0.023,0.364,-1.329/
MOVEL=-101.198,-5.527,0.326,-0.020,0.364,-1.329/
MOVEL=-101.198,-4.522,0.325,-0.016,0.364,-1.329/
```

(a) (b) (c)

Fig. 6. Modeling procedure for timevarying machining stiffness under complex machining interactions. (a) Details of the compliance coordinate system and the Frenet frame. (b) Visualization of motion interaction mechanism. (c) Illustration for framework of dwell time planning correction.

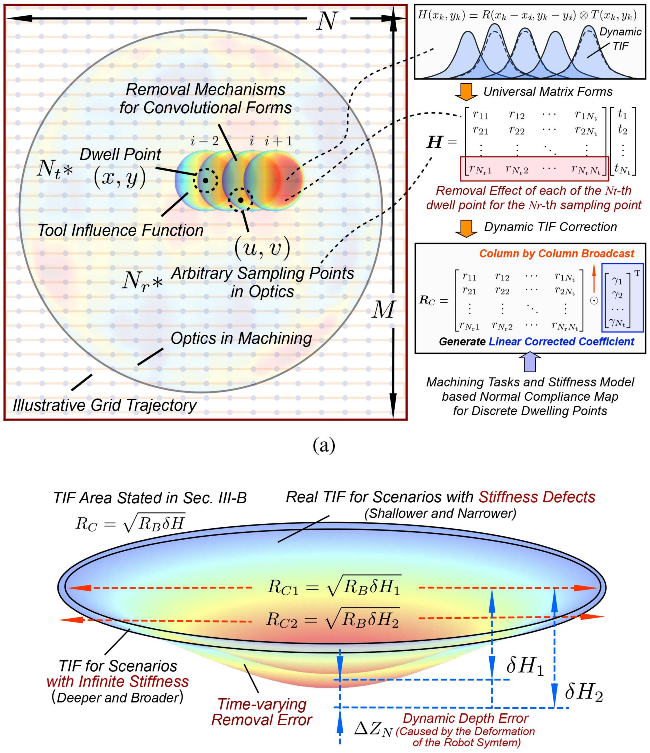

(a)

(b)

Fig. 7. Demonstration of the dwell time correction process. (a) Illustration of the dwell time correction method considering the dynamic TIF and CCOS convolution effect. (b) Simplification of the difference between ideal TIF and actual TIF to facilitate the calculation of the modified effect matrix $\boldsymbol{R}$.

where $\mathscr{X}_i$ and λ_i denote the eigenvectors and corresponding eigenvalues. Due to the elastic adjustment of the actuator, the normal support force on the tool is decomposed into a constant actuator reaction force as well as a breakdown force. As illustrated in Fig. 6(b), a compliance subspace perpendicular to the actuator reaction force is created from the eigenvectors. Based on the projection of $\mathrm{Span}(\mathscr{X}_1, \mathscr{X}_2)$ onto the normal vector derived from the Frenet frame, neglecting the impact of tool axis compliance on the undesired polishing offset, the linear equivalent compliance in the normal direction yields

$$\begin{aligned} \mathscr{C}_{\mathrm{LE}}^{\mathrm{Norm}} &= \lambda_1 \mathrm{Proj}_{\boldsymbol{b}_i} \mathscr{X}_1 + \lambda_2 \mathrm{Proj}_{\boldsymbol{b}_i} \mathscr{X}_2 \\ &= \lambda_1 \langle \mathscr{X}_1, \boldsymbol{b}_i \rangle \, \boldsymbol{b}_i + \lambda_2 \langle \mathscr{X}_2, \boldsymbol{b}_i \rangle \, \boldsymbol{b}_i. \end{aligned} \tag{43}$$

Considering that the primary source of the normal support force on the tool is the deformation of the robot system, the offset error caused by the time-varying discrete normal linear compliance $\mathscr{C}_{\mathrm{LE}}^{N}$, under the constant loading force F_V provided by the voice coil actuator, can be determined as

$$\Delta z_{\mathrm{Norm}} = \mathscr{C}_{\mathrm{LE}}^{\mathrm{Norm}} F_V / \cos(\varphi) \propto \mathscr{C}_{\mathrm{LE}}^{\mathrm{Norm}} \tag{44}$$

where Δz_N and φ represents the error in polishing offset caused by robot deformation and the tool dip, respectively. Therefore, we can obtain the time-varying TIF residuals that account for the derivative effects of LSF errors caused by time-varying contact compliance related to machining tasks, considering the imbalance stiffness deficiencies of the robot

$$\mathrm{TIF}_{\mathrm{Res}}(x, y) = \mathrm{TIF}_{\mathrm{Exp}}(x, y) - \mathrm{TIF}_{\mathrm{Real}}(x, y). \tag{45}$$

where the TIF under scenarios with infinite and undesired stiffness defects at the referenced dwell point in the machining trajectory can be attained from Section II-B, respectively.

D. Optimized Removal Map-Based Dwell Time Correction

Within the optical surface machining process, the optical surface error detected from the interferometer is denoted by $S(x_k, y_k)$. Simultaneously, the removal effect stemming from the action of the polishing tool upon the optics is expressed as $R(x_k - u_i, y_k - v_i)$. The disparity between the anticipated and actual surface is defined as the surface form residuals

$$E(x_k, y_k) = S(x_k, y_k) - H(x_k, y_k) \tag{46}$$

where $H(x_k, y_k) = R(x_k - u_i, y_k - v_i) \otimes T(x_k, y_k)$. The symbol $\otimes$ represents the material convolutional removal mechanism governed by the TIF and dwell time. We rewrite (46) to convert the dwell time deconvolutional solution to the matrix form, considering that the time-varying TIF in the bonnet polishing process is composed of the ideal time-invariant TIF in an infinite stiffness scenario and the residuals of the time-varying TIF, as illustrated in Fig. 7(a)

$$\boldsymbol{H} = \boldsymbol{R}\boldsymbol{T} = (\boldsymbol{R}_0 + \delta \boldsymbol{R}) \, \boldsymbol{T} \in \Re^{N_r}$$

$$\boldsymbol{H}=\begin{bmatrix} h_1 \\ h_2 \\ \vdots \\ h_{N_\mathrm{r}} \end{bmatrix}, \boldsymbol{R}_0=\begin{bmatrix} r_{11} & r_{12} & \cdots & r_{1N_\mathrm{t}} \\ r_{21} & r_{22} & \cdots & r_{2N_\mathrm{t}} \\ \vdots & \vdots & \ddots & \vdots \\ r_{N_\mathrm{r}1} & r_{N_\mathrm{r}2} & \cdots & r_{N_\mathrm{r}N_\mathrm{t}} \end{bmatrix}, \boldsymbol{T}=\begin{bmatrix} t_1 \\ t_2 \\ \vdots \\ t_{N_\mathrm{t}} \end{bmatrix} \tag{47}$$

where the variants N_r and N_t denote the index of trajectory points and sampling points on the optics. Unfortunately, obtaining the effect matrix residuals for each dwell point is challenging, as it requires complex and computationally intensive calculations for each specific position. To address this, we introduce a novel approach using a linearly corrected TIF that significantly reduces computational demands on computational resources. Revisiting the dynamic TIF residuals for each dwell position discussed in Section III-C, we analyze them from a fresh perspective. As illustrated in Fig. 7(b), the current TIF in bonnet polishing follows a Gaussian-like distribution, in which, according to the Lyda criterion, the majority of material removal occurs in the central region rather than at the edges. Consequently, based on the Preston Formula, the dynamic TIF variation resulting from undesired deformations due to robot stiffness deficiencies can be approximated as follows:

$$\frac{\mathrm{TIF}_{\mathrm{Real}}}{\mathrm{TIF}_{\mathrm{Exp.}}}=\frac{V_{\mathrm{Real}}}{V_{\mathrm{Exp.}}}\approx\frac{\delta H_1}{\delta H_2}=1-\frac{\Delta Z_N}{\delta H_2}=\gamma\in(0,1) \tag{48}$$

where γ represents the corrected coefficient at the referenced sampling point. Thus, we can assess the deviation of each position in the effect matrix $\boldsymbol{R}$ w.r.t the ideal TIF and apply corrections. Hence, the ingenious corrected process yields

$$\boldsymbol{R}=\boldsymbol{R}_0\odot\boldsymbol{\gamma}^{\dagger}=\begin{bmatrix} r_{11} & \cdots & r_{1N_\mathrm{t}} \\ r_{21} & \cdots & r_{2N_\mathrm{t}} \\ \vdots & \ddots & \vdots \\ r_{N_\mathrm{r}1} & \cdots & r_{N_\mathrm{r}N_\mathrm{t}} \end{bmatrix}\odot\begin{bmatrix} \gamma_1 \\ \gamma_2 \\ \vdots \\ \gamma_{N_\mathrm{t}} \end{bmatrix}^{\mathrm{T}} \tag{49}$$

where the symbol $\odot$ denotes the Hadamard product operator, performing broadcast column by column on the matrix $\boldsymbol{R}_0$.

When the bonnet tool dwells on a particular trajectory point for polishing during the machining process, the sparsity of the matrix $\boldsymbol{R}$ is considerable due to the large number of trajectory points N_t and sampling points N_r, while the effective material removal area is negligible in comparison to the machining area. The Tikhonov regularization is introduced to reduce the ill-conditioning of (47), and the dwell time optimization problem is further expressed as follows:

$$\begin{aligned} &\min && \left(\sum_{k=1}^{N_\mathrm{r}}\left[\sum_{j=1}^{N_\mathrm{t}}\left(r_{kj}^{C}t_j-h_k\right)^2\right]/N_\mathrm{r}+\mathcal{P}\sum_{j=1}^{N_\mathrm{t}}t_j^2\right) \\ &\text{s.t.} && \forall j,\ t_j\geq 0 \end{aligned}$$

where $\mathcal{P}$ denotes the regularization factor for stable solutions. Thus far, we complete the overall description of the proposed method for correcting surface form errors caused by dynamic TIF due to the stiffness defects, without altering the existing hardware conditions or the dwell time solution algorithm.

TABLE I
BASIC PERFORMANCE SPECIFICATIONS OF THE CCOS ROBOT

Item/ Metric	Details
Number of Motion Axes	5 (3 in parallel section & 2 in series section)
U$\underline{P}$S Limb Available Working Length	950-1750 mm
Workspace Radius	660 mm
Workspace Height	200-910 mm
Position Accuracy	0.0591 mm
Orientation Accuracy	0.0183 Deg

IV. EXPERIMENT AND RESULT DISCUSSION

In this section, several experiments were conducted on an optical machining robot platform equipped with a bonnet polishing machining system and high-precision optical measurement instruments. The experiments included the following:

1) validation of the equivalent compliance spatial field of the robot tool center point;
2) verification of the bonnet polishing TIF under different machining parameters;
3) validation of the proposed dwell time compensation method based on the robot dynamic task-independent compliance and dynamic TIF through multiple practical polishing tasks in Sim2Real cases.

A. General Deployment and Instruments Layout

The details of the optical machining robot and its end effector (CCOS machining system) are illustrated in Fig. 8(a). The optical machining robot primarily consists of three identical active U$\underline{P}$S limbs and one redundant constrained passive UP limb, along with a moving platform and a 2-DoF A/C wrist assembly. The workspace dimensions and relevant performance parameters of the robot are outlined in Table I. Fig. 8(b) and (c) illustrates the details of the CCOS machining system, primarily consisting of a servo motor for bonnet polishing, a machining spindle, and a voice coil actuator, as shown in Fig. 9. When energized, the electromagnetic coil can apply axial polishing pressure to the ball-end tool. Simultaneously, the bonnet tool operates at a fixed angle relative to the normal vector of the optical surface, ensuring a constant TIF during the machining process while maintaining a constant polishing pressure and tangential velocity field in the sliding contact zone.

B. Linear Compliance Field Experimental Validation

To assess the performance of the spatial discrete linear compliance field, static stiffness experiments were conducted on the aforementioned hardware platform. Stiffness loading was performed on the experimental optical surfaces in different positions using a reference tool at various orientations. Specifically, varying degrees of displacement were applied to the surface normal, and the stable force sensor readings after displacement application were recorded. In addition, the linear compliance numerical model outlined in Section III-C was utilized to calculate the linear compliance coefficient at each reference pose, and the differences were compared with the measured values. Fig. 10 illustrates the correlation between the measurement values and numerical calculations of the discrete

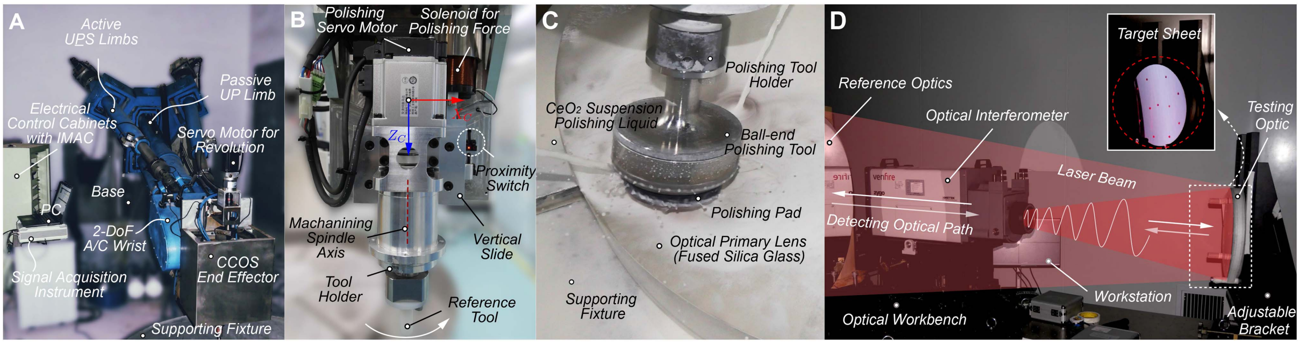

Fig. 8. General deployment of the experiment setup. (a) 5-DoF polishing robot and the pertinent instruments. (b) Details of the CCOS servo system for polishing optics. (c) Illustration of the polishing process for the optical primary lens. (d) Instrument layout for testing polished optics.

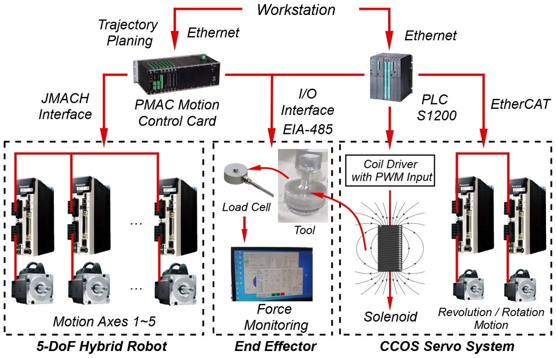

Fig. 9. Layout and the deployment details of the hardware with in the mechatronic system for high-precision CCOS machining.

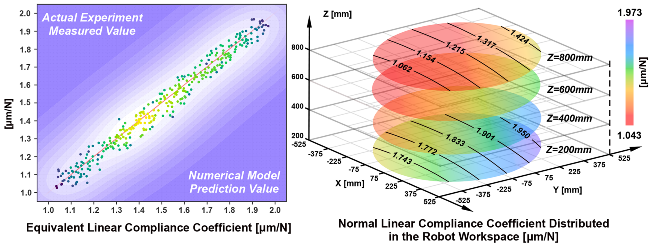

Fig. 10. Compliance results for loaded point locations in the robot workspace, compared with the numerical models within Section III-C.

TABLE II
PARAMETERS SETUP DETAILS FOR THE VALIDATION OF THE PROPOSED CONTACT-REMOVAL NUMERICAL MODEL

S/N	Symbol	Parameter Description	Value Set
1	k	Preston's Constant [a]	1.49E-9
2	E_r	Young's Modulus of Polyurethane	29.6 Mpa
3	ν_r	Poisson's Ratio of Polyurethane	0.40
4	λ	Lamé's First Parameter	42.29 Mpa
5	μ	Dynamic Viscosity of Polyurethane LP66	2.00E-4 Mpa·s
6	η	Second Viscosity of Polyurethane LP66	0.80E-4 Mpa·s
7	E_R	Young's Modulus of the Fused Silica	70.5 Gpa
8	ν_R	Poisson's Ratio of the Fused Silica	0.16

[a] The Preston constant here is set with the optical material as fused silica glass, the polishing pad as polyurethane LP66, the abrasive as 1.5μm (max) CeO$_2$@15wt.%.

linear compliance at various loading points. It also shows the distribution of numerical discrete compliance at different positions within the workspace, demonstrating a close alignment between the discrete linear compliance theoretical model based on the previous methodology and the actual scenario. The values of actual linear compliance fall within the range of 1.04–1.97μm/N, with mean average percentage error and maximum percentage error being 4.19% and 6.38% , respectively, thereby validating the accuracy of the theoretical model. In addition, the vertical compliance stiffness of the robot exhibits continuous variation throughout the workspace, displaying significant nonuniformity both within planes at different vertical heights and within planes at the same numerical height. Hence, during polishing operations conducted by the optical processing hybrid robot, fluctuations in compliance resulting from changes in the dwell point along the execution trajectory are inevitable. In the absence of dwell time correction, there is a significant risk of uncertainty regarding removal errors due to dynamic TIF caused by compliance changes during high-precision optical polishing. The presence of these fluctuations is one of the primary factors contributing to LSF errors components on the optics.

C. Evaluation of the Contact-Removal Model

To evaluate the precision performance of the proposed generic TIF formula for optical surface materials under varying polishing pressures and speeds, six groups of fixed-spot polishing experiments were conducted on experimental optical surfaces. To minimize random errors in the measurements, each fixed-point polishing experiment was repeated five times for each parameter setting. The specific environmental parameters and physical constants set in the numerical computational model are presented in Table II. To mitigate the occurrence of black border effects at the polishing contact boundary during interferometric detection by a Zygo GPI laser interferometer at higher material removal levels, the DUI Nanomefos 600S optical detection instrument was utilized to replace the GPI laser interferometer for detecting the planar contour after a specific duration of fixed-point polishing. Fig. 11(b) presents the inspection results and the normalized cross-sectional profiles along the X- and Y-axes following fixed-point polishing. Subsequently, the percentage error of maximum depth and volume removed within

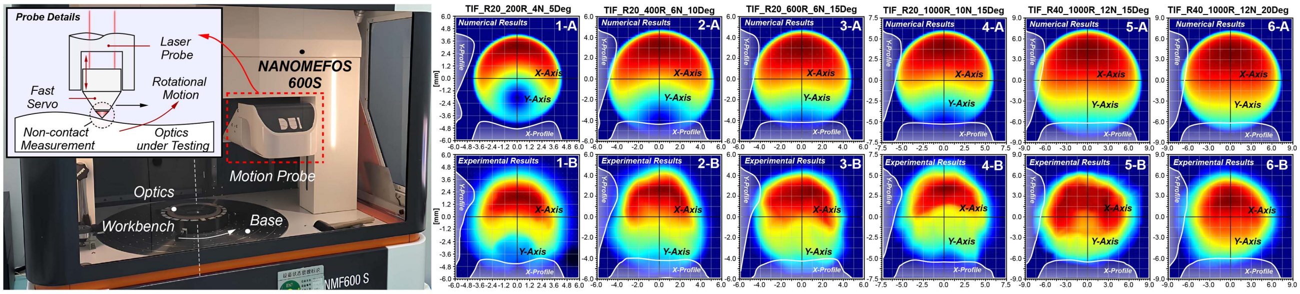

(a) (b)

Fig. 11. Validation of the contact-removal model. (a) The detection process. (b) Results comparison and normalized crosssectional profiles.

TABLE III
SCENARIO LAYOUT DETAILS AND CONTOUR RESULTS FOR THE FIXED SPOT POLISHING REMOVAL EXPERIMENT IN SECTION III WITH A DURATION OF 1 MIN, COMPARED WITH THE NUMERICAL MODEL

S/N	Size	Speed	Force	Tool Dip	D_{MAX}-PE/ %	V-PE/ %	Avg. JSD/ -
1	20 mm	200 rpm	4 N	5 Deg	3.204%	4.114%	0.298
2	20 mm	400 rpm	6 N	10 Deg	2.965%	3.822%	0.255
3	20 mm	600 rpm	6 N	15 Deg	2.232%	4.704%	0.206
4	20 mm	1000 rpm	10 N	15 Deg	2.377%	4.046%	0.172
5	40 mm	1000 rpm	12 N	15 Deg	2.604%	3.930%	0.107
6	40 mm	1000 rpm	12 N	20 Deg	3.971%	4.184%	0.132

the clear aperture, along with the Jensen–Shannon divergence of normalized cross-sectional profile distributions, are reported in Table III. Notably, the numerical results for the fixed-point polishing experiments accounted for and corrected the effects of robot stiffness defects on the TIF. The results clearly indicate that the experimentally obtained removal spot shapes closely align with those predicted by numerical model. Across various parameter settings, the removal spots exhibit a bivariate Gaussian distribution. The profile along the X-axis generally shows an M-shape, while the profile along the Y-axis presents a skewed Gaussian distribution due to the combined effects of tool dip and asymmetric dissipative stress. This alignment in profile further validates the precision of the contact-removal model discussed in Section III-A.

To better visualize the adverse effects of dynamic TIF on optics, specifically due to variations in the robot's dwell posture during the machining process, we conducted a brief experiment on a cylindrical lens that had previously been shaped by magnetorheological finishing. To highlight the differences in evolutionary TIF, we polished the surface using identical dwell times, repeating the process ten times to obtain more intuitive detection results. Theoretically, the removal depth across the clear aperture should be uniform. However, post-polishing measurements unexpectedly revealed inconsistencies in material removal, leading to a significant increase in surface error, as illustrated in Fig. 12. Furthermore, we compared the correction coefficient reshape distribution γ, calculated in Section III-D for the task, with the removal depth distribution. The alignment of these distributions underscores the necessity of applying lower coefficients in regions with insufficient material removal to expand the dwell time and mitigate surface errors.

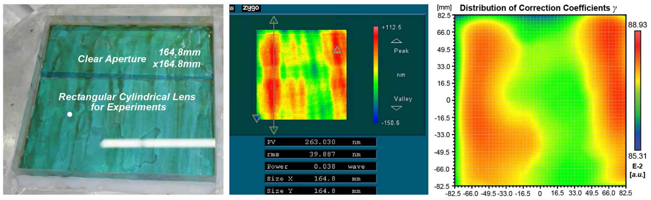

PV 263.030 nm
rms 39.887 nm
Power 0.038 wave
Size X 164.8 mm
Size Y 164.8 mm

Fig. 12. Visualization of the adverse influence of dynamic TIF.

D. Sim2Real Demonstration: Hybridization Design

The current real-world comparative experiments for optimizing dwell time in optical processing face significant challenges. Given the inherent complexities of process characteristics and machining processes, obtaining two identical surfaces for a controlled comparative environment is virtually impossible. To address this challenge, a dual approach was employed. First, the differences between algorithms were validated through numerical simulations, emphasizing variations in dwell time distribution to ensure an objective comparison. Second, a hybrid approach was utilized in the practical processing experiments. This involved minimizing clamping errors and standardizing process parameters to the greatest extent possible, thereby creating a stable comparison environment that enabled various comparison tasks to be conducted on the same optical surface. During the finishing stage, the difficulty of surface error convergence varies depending on different precision levels. Consequently, the sequence of comparative machining tasks was adjusted accordingly. The original intention of this comparative experimental design was to demonstrate the effectiveness of the proposed method by achieving faster and more robust convergence in higher precision machining stages. Therefore, to further verify the effectiveness of the proposed method in suppressing LSF errors while achieving accelerated convergence for optical processes, a set of comparative experiments was conducted under various scenarios in a real-world environment. The experimental scenarios were designed as follows:

1) without compensation;
2) with competitive methods [17];
3) with the proposed method.

To ensure a fair assessment of the convergence performance of the comparison methods, all methods uniformly adopted

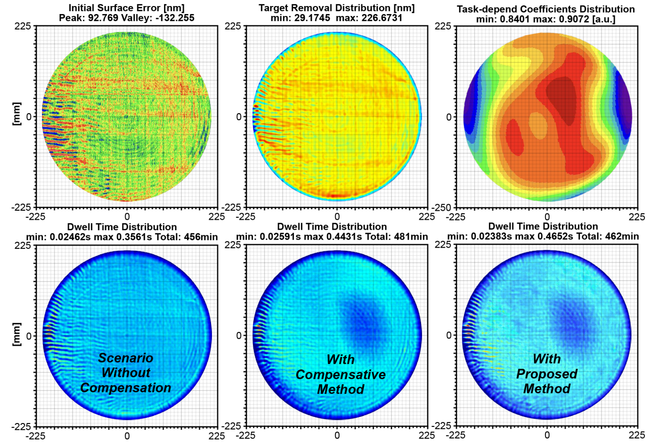

Fig. 13. Dwell time distribution results under simulation demonstration.

TABLE IV
DETAILS OF THE COMPARISON METHOD UTILIZED AND THE FINAL RESULTS OF THE SIMULATION DEMONSTRATION

Task S/N	Applied TIF	Compensation Method	CCOS Convolution	Solution Method	Reconstruction Error Metrics [nm]
1	Static	NaN.	Fit	MIM	PV: 16.81 RMS: 5.62
2	Dynamic	Upon reference dwell time.	Unfit	MIM	PV: 8.91 RMS: 4.95
3	Dynamic	Upon dynamic TIF.	Fit	MIM	PV: 6.57 RMS: 1.93

the matrix-form-based MIM method for calculating dwell time distribution [23].

1) Simulation Demonstration: To objectively evaluate the performance of the three scenarios, the same initial surface error profile was utilized in the simulation-based demonstration. In detail, consistent task parameters were established, including a TIF with a radius of 20 mm, a speed of 1000 r/min, a tool tilt angle of 15°, a polishing pressure of 12 N, a grid trajectory spacing and dwell intervals of 1 mm, and identical workpiece coordinate system settings. Fig. 13 illustrates the initial surface error, the target material removal distribution, and the corresponding dwell time distributions for each scenario. In addition, the correction coefficient distribution related to the task was provided to highlight the relationship between dynamic TIF and dwell time correction. The results indicate that both the competitive method and the proposed approach adjusted the dwell time distribution to address removal errors caused by dynamic TIF under conditions of stiffness deficiency. Table IV outlines the detailed differences between the three methods and their respective removal reconstruction errors. The proposed method significantly outperformed both the uncompensated scenario and the competitive method. Although the competitive method demonstrated some improvement over the uncompensated approach, it introduced considerable root mean square (RMS) error due to its failure to account for convolution effects.

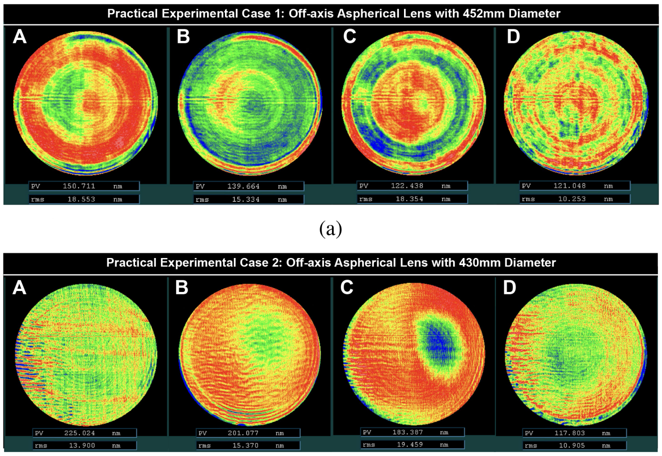

(a)

(b)

Fig. 14. Real-world cases of optical fabrication with hybridization design. (a) Hybridization experiments for each scenario in real-world Case 1. (b) Hybridization experiments for each scenario in real-world Case 2.

TABLE V
COMPARISON OF OPTICAL SURFACE ERROR CONVERGENCE PROCESSES

Scenarios Setup / Surface Form Error Metric [nm]	**CASE 1** PV	RMS	**CASE 2** PV	RMS
Initial Surface (A)	150.711	18.533	225.024	13.902
With Competitive Method [17]	–7.33%	–17.26%	–10.64%	+10.58%
Surface Result (B)	139.664	15.334	201.077	15.377
Without Compensation	–12.33%	+19.69%	–8.80%	+26.60%
Surface Result (C)	122.438	18.354	183.387	19.459
With Proposed Method	**–1.14%**	**–44.14%**	**–35.76%**	**–43.96%**
The Final Surface (D)	**121.048**	**10.253**	**117.803**	**10.905**

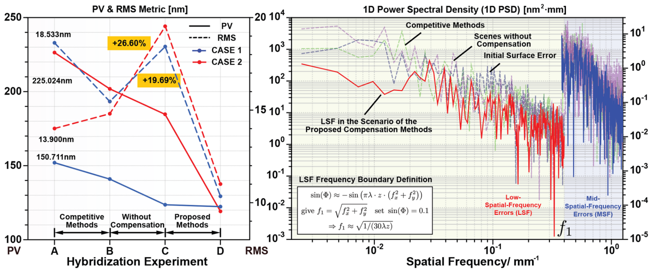

Fig. 15. PV and RMS metrics and PSD enhancement for the cases.

2) Practical Verification: As illustrated in Fig. 14, two off-axis aspheric lenses with diameters of 452 and 430 mm were utilized in the practical validation cases. The processing parameters employed were identical to those in the simulation environment. Based on the detection results observed upon the real-world experiments illustrated in Table V and Fig. 15, it was found that, without compensation, the convergence rates for both peak-to-valley (PV) and rms errors were mediocre across both lenses. While the both cases demonstrated some improvement in the PV value, the rms index exhibited negative convergence, suggesting that, without compensation, the removal distribution deviated significantly from the intended profile due to complex variations in machining compliance. This instability ultimately led to increased surface morphology errors. Conversely, the application of competitive methods resulted in nonrobust convergence of rms errors for both lenses. In Case 2 with lower rms, the competitive method further exacerbated the rms errors for surface B. This unexpected outcome arises from the linear correction approach for single dwell point times employed by the competitive method, which does not account for the convolution effects inherent in CCOS. Consequently, when adjacent dwell points with similar correction coefficients encounter localized peaks and valleys, the risk of increased removal errors is significantly heightened. Although the competitive method adversely affected the rms metric, it did manage to address low-frequency errors induced by dynamic TIF under varying machining conditions, as reflected in the PV metric. In contrast, the proposed method, which incorporates dynamic TIF compensation based on the machining trajectory, achieved effective convergence for both PV and rms metrics from surface C to surface D, demonstrating superior correction capabilities for the high-precision optical surface form errors.

Fig. 15 illustrates the power spectral density (PSD) changes for four surface phases in practical Case 2, as defined by Parseval's theorem. The proposed method demonstrates a significant improvement in power spectral intensity over the other three surfaces within each spectrum of LSF errors, showcasing its strong capability to suppress LSF errors. In addition, while the method demonstrates some degree of suppression for intermediate-frequency error components, further postprocessing techniques, such as magnetorheological finishing, are still necessary to achieve suppression comparable to that of LSF errors. Overall, the proposed method facilitates rapid convergence of surface errors, substantially reducing the time required for the subsequent precision polishing stage, which is typically less robust and more time-consuming, thereby enhancing the efficiency and stability of the optical fabrication.

V. CONCLUSION

To address low-frequency spatial errors in polishing processes arising from task-related stiffness deficiencies and resulting uncertainties in polishing dwell time, this study proposes a novel dwell time correction framework that accounts for these processing uncertainties. The framework quantifies and corrects the uncertainties in dwell time through an in-depth exploration of the compliance field of the polishing task and the motion interactions of the Frenet frame under the machining task. The effectiveness of the proposed method is validated through real experiments, demonstrating strong suppression of low-frequency spatial errors when accounting for these uncertainties, thus outperforming the State-of-the-Art method. Future work will concentrate on exploring virtual reality environments using agent-based interaction models to simulate the formability of optically machined robots, with the aim of implementing an integrated digital twin approach.

REFERENCES

[1] M. S. Turner, "Extremely large telescopes at risk," *Science*, vol. 382, no. 6673, 2023, Art. no. 857.

[2] S. Kruk et al., "The impact of satellite trails on Hubble Space Telescope observations," *Nature Astron.*, vol. 7, no. 3, pp. 262–268, 2023.

[3] J. Li, G. Cheng, and Y. Pang, "A novel deep learning-based spatio-temporal model for prediction of pose residual errors in optical processing hybrid robot," *IEEE Trans. Ind. Inform.*, vol. 20, no. 6, pp. 8749–8762, Jun. 2024.

[4] C. Hu et al., "Specifications and control of spatial frequency errors of components in two-beam laser static holographic exposure for pulse compression grating fabrication," *High Power Laser Sci. Eng.*, vol. 12, 2024, Art. no. e1.

[5] S. Chen, T. Lin, H. Feng, Z. Xu, Q. Li, and Y. Chen, "Computational optics for mobile terminals in mass production," *IEEE Trans. Pattern Anal. Mach. Intell.*, vol. 45, no. 4, pp. 4245–4259, Apr. 2023.

[6] J. Li, Y. Guan, H. Chen, B. Wang, and T. Zhang, "Robotic polishing of unknown-model workpieces with constant normal contact force control," *IEEE-ASME Trans. Mechatron.*, vol. 28, no. 2, pp. 1093–1103, Apr. 2023.

[7] R. Pan et al., "Evaluation of removal characteristics of bonnet polishing tool using polishing forces collected online," *J. Manuf. Process.*, vol. 47, pp. 393–401, 2019.

[8] R. Pan et al., "Qualitative motion control optimization of the pad dressing process for bonnet tool," *IEEE-ASME Trans. Mechatron.*, vol. 24, no. 3, pp. 1141–1152, Jun. 2019.

[9] Z. Wu et al., "Research on polishing aluminum alloy optical elements with a new solid flexible bonnet tool," *J. Manuf. Process.*, vol. 103, pp. 168–180, 2023.

[10] B. Zhong, W. Deng, X. Chen, S. Wen, J. Wang, and Q. Xu, "Frequency division combined machining method to improve polishing efficiency of continuous phase plate by bonnet polishing," *Opt. Exp.*, vol. 29, no. 2, pp. 1597–1612, 2021.

[11] Z. Huang, G. Chen, H. Liu, Z. Rao, and J. Wu, "Research on robot bonnet polishing silicon carbide optical element machining method based on improved traveling salesman problem pseudo-random polishing path planning," *Opt. Eng.*, vol. 61, no. 2, 2022, Art. no. 25102.

[12] R. Pan et al., "Research on an evaluation model for the working stiffness of a robot-assisted bonnet polishing system," *J. Manuf. Process.*, vol. 65, pp. 134–143, 2021.

[13] J. Zhang and H. Wang, "Generic model of time-variant tool influence function and dwell-time algorithm for deterministic polishing," *Int. J. Mech. Sci.*, vol. 211, 2021, Art. no. 106795.

[14] Y. Zhang, J. Feng, Y. Zhao, M. Rao, and Y. Yin, "Towards understanding and restraining the mechanical relaxation effect in polishing silicon carbide with a detachable bonnet tool," *Int. J. Mech. Sci.*, vol. 246, 2023, Art. no. 107962.

[15] Z. Wang et al., "Modelling of polyurethane polishing pad surface topography and fixed-point polished surface profile," *Tribol. Int.*, vol. 195, 2024, Art. no. 109646.

[16] D. Liao, F. Zhang, R. Xie, S. Zhao, J. Wang, and Q. Xu, "Deterministic control of material removal distribution to converge surface figure in full-aperture polishing," *J. Manuf. Process.*, vol. 53, pp. 144–152, 2020.

[17] X. Huang, Z. Wang, L. Li, and Q. Luo, "Research on the modification of the tool influence function for robotic bonnet polishing with stiffness modeling," *Robot. Comput.-Integr. Manuf.*, vol. 86, 2024, Art. no. 102674.

[18] C. Lv, L. Zou, Y. Huang, H. Li, T. Wang, and Y. Mu, "A novel toolpath for robotic adaptive grinding of extremely thin blade edge based on dwell time model," *IEEE-ASME Trans. Mechatron.*, vol. 27, no. 6, pp. 4429–4439, Dec. 2022.

[19] P. Ji, D. Li, Y. Jin, X. Su, and B. Wang, "Compensation of the tool influence function changes under neighborhood effect in atmospheric pressure plasma processing," *Opt. Exp.*, vol. 31, no. 24, pp. 39465–39482, 2023.

[20] R. Wang, Z. L. Li, Z. Fan, X. Q. Zhang, M.-J. Ren, and L.-M. Zhu, "Surrogate-model-based dwell time optimization for atmospheric pressure plasma jet finishing," *Int. J. Mech. Sci.*, vol. 281, 2024, Art. no. 109547.

[21] K. L. Johnson, *Contact Mechanics*. Cambridge, U.K.: Cambridge Univ. Press, 1985, pp. 11–106.

[22] D. J. Acheson, *Elementary Fluid Dynamics*. Oxford, U.K.: Oxford Univ. Press, 1990, pp. 201–220.

[23] T. Wang et al., "A comprehensive review of dwell time optimization methods in computer-controlled optical surfacing," *Light, Adv. Manuf.*, vol. 5, no. 21, pp. 422–451, 2024.

Jun Li (Graduate Student Member, IEEE) received the M.Sc. degree in mechanical design and theory in 2019 from the China University of Mining and Technology, Xuzhou, China, where he has been working toward the Ph.D. degree in mechanical engineering since 2020.

His research interests include cyber-physical systems (CPS) fusion theory, deep-learning-based robotics, and advanced optics.

Dr. Li is a Member of the IEEE Industrial Electronic Society (IES) and IEEE Robotics and Automation Society (RAS).

Gang Cheng received the B.Sc. degree in mechanical design and theory from Wuhan University, Wuhan, China, in 2000, the M.Sc. degree in optoelectronics engineering from the Institute of Optics and Electronics, Chinese Academy of Sciences, Chengdu, China, in 2003, and the Ph.D. degree in mechanical design and theory from the China University of Mining and Technology, Xuzhou, China, in 2008.

He currently works as a Professor with the China University of Mining and Technology. He is currently involved in research on robotics and fault diagnosis of mechatronics.

Dr. Cheng is a Member of the American Society of Mechanical Engineers (ASME).

Bin Fan received the Ph.D. degree in optical engineering from the Institute of Optics and Electronics, Chinese Academy of Sciences, Chengdu, China, in 2006.

He worked as a Visiting Scholar with the University of Arizona, Tucson, AZ, USA, in 2010. He currently works as a Research Fellow with the Institute of Optics and Electronics, Chinese Academy of Sciences. His research interests include advanced optical manufacturing technology and diffraction imaging technology.

Dr. Fan is a Member of Society of Photo-Optical Instrumentation Engineers (SPIE).

Yusong Pang received the M.Sc. degree in electrical engineering from the Taiyuan University of Technology, Taiyuan, China, in 1996, and the Ph.D. degree in intelligent belt conveyor monitoring and control from the Delft University of Technology, Delft, The Netherlands, in 2007.

In 2010, he was appointed as an Assistant Professor with the Department of Transport Engineering and Logistics, Delft University of Technology. His current research interest include the intelligent control for large-scale material handling systems and logistics processes.